atmosphere

Article

Analysis of the Severe Dust Process and Its Impact on Air Quality in Northern China

Xiaoyu Liu [1,2], Yu Zhang [1,2,3,*], Hailan Yao [1,2], Qinlai Lian [1,2] and Jianjun Xu [3]

1 Key Laboratory of Climate, Resources and Environment in Continental Shelf Sea and Deep Sea of Department of Education of Guangdong Province, Laboratory for Coastal Ocean Variation and Disaster Prediction, College of Ocean and Meteorology, Guangdong Ocean University, Zhanjiang 524088, China; liuxiaoyu@stu.gdou.edu.cn (X.L.); yaohailan2000@163.com (H.Y.); lianqinlai@stu.gdou.edu.cn (Q.L.)
2 Key Laboratory of Space Ocean Remote Sensing and Application, Ministry of Natural Resources, Beijing 100032, China
3 CMA-GDOU (China Meteorological Administration-Guangdong Ocean University) Joint Laboratory for Marine Meteorology, South China Sea Institute of Marine Meteorology, Guangdong Ocean University, Zhanjiang 524088, China; jxu@gdou.edu.cn
* Correspondence: zhangyu@gdou.edu.cn

Abstract: Extreme meteorological events can influence air quality. In March 2021, northern China experienced a severe dust event, leading to widespread air quality deterioration. Using reanalysis datasets and station data, we investigate the synoptic weather patterns, dust transport characteristics, and associated impacts on air quality during this event. The results are as follows. (1) The dust event is closely linked to the Mongolian cyclone, providing favorable conditions for dust emission and long-distance transport. (2) The Gobi Desert in Mongolia is the primary source, with dust particles transported from Mongolia to northern China via the northwesterly flow. Dust transport exhibits a complex three-dimensional structure, with the most intense dust transport at approximately 2500 m altitude. (3) The impact of this dust event on air quality was characterized by its remarkable intensity, extensive spatial coverage, and prolonged duration. Additionally, 58.8% of the stations in northern China experienced pollution, 36.3% of them reached severe pollution levels or higher, and 35.9% of the sites experienced more than 12 h of pollution. (4) The visibility at the northern stations near the dust source rapidly decreases due to solid dust particles. In contrast, the southern stations, with higher moisture content, are primarily affected by liquid particles in terms of visibility. After the frontal passage, wet deposition from the precipitation process gradually improves visibility.

Keywords: sandstorm; air quality; three-dimensional transport; PM_{10}

Citation: Liu, X.; Zhang, Y.; Yao, H.; Lian, Q.; Xu, J. Analysis of the Severe Dust Process and Its Impact on Air Quality in Northern China. *Atmosphere* **2023**, *14*, 1071. https://doi.org/10.3390/atmos14071071

Academic Editor: Min Shao

Received: 20 May 2023
Revised: 21 June 2023
Accepted: 23 June 2023
Published: 25 June 2023

1. Introduction

Air pollution is a significant environmental issue that many countries face in their development, affecting various aspects such as human health, socio-economics, and the ecological environment [1,2]. The impact of air quality deterioration on human health is the most severe, as long-term exposure to environments with excessive particulate matter 10 (PM_{10}) can increase mortality and morbidity rates [3]. To address these problems, the Chinese government has introduced a range of policies and regulations aimed at controlling air pollution, including the 'Ten Measures for Air Pollution Prevention and Control Action Plan' and the 'Three-Year Action Plan to Win the Battle for Blue Sky Protection', which prioritize the need to tackle health and ecological problems caused by particle pollution. A comprehensive and proactive approach has led to significant improvements in China's air quality over the past decade [4,5]. However, in addition to anthropogenic factors, extreme natural disasters may have a significant impact on the progress made in improving air quality. For instance, in northern China, the air quality significantly deteriorates during extreme weather events such as sandstorms [6].

The sandstorm is a meteorological phenomenon characterized by strong winds lifting a large amount of dust and sand from the ground into the air, resulting in horizontal visibility dropping below 1 km. It is prevalent during spring and has serious harm to human health, the ecological environment, and transportation systems. The major dust sources in East Asia are located in arid and semi-arid regions, including the Gobi Desert, Taklamakan Desert, and Hexi Corridor. Among them, the Gobi Desert in Mongolia contributes the most. Although the Taklamakan Desert has the largest dust emission capacity, the dust is generally not easily transported outward because the Tarim Basin is surrounded by mountains on three sides [7,8]. The occurrence of dust events requires favorable underlying surface conditions and a conducive weather background [9,10], with strong winds being the main driving force for sand lifting and long-distance transport [11]. As a result of dust transport, the concentration of PM_{10} in the atmosphere increases significantly, and both near-surface visibility and air quality are reduced [12]. Therefore, analyzing the dust transport process is crucial for exploring the evolution of near-surface air quality.

The transport of dust exhibits significant three-dimensional characteristics. However, due to limitations in observational data, a considerable amount of research has primarily focused on the horizontal transport characteristics of dust in a two-dimensional plane [13,14]. Numerical models can provide three-dimensional parameters, but they are highly sensitive to initial and boundary conditions when simulating sand and dust transport processes. Most simulations still have shortcomings in accurately representing the dust emission process, resulting in lower confidence in the simulation outcomes [15,16]. Reanalyzed data, which assimilate multiple sources of dust observations, including ground-based, sounding, and satellite data, can provide powerful support for analyzing the three-dimensional transport of dust. The global Copernicus Atmospheric Monitoring Service (CAMS) reanalysis of atmospheric composition, provided by the European Center for Medium-Range Weather Forecasts (ECMWF), is the latest generation of global atmospheric composition reanalysis products. This dataset exhibits improved quality and higher resolution compared to its predecessors [17,18]. Some researchers have successfully used this data for analyzing dust processes and have obtained reliable results [19].

Due to climate change, wind speeds in East Asia have decreased over the past few decades [20], while soil moisture has increased and vegetation coverage has improved [21,22]. As a result, the overall trend in East Asian dust activity has exhibited a weakening tendency, with significant decreases in the number of dusty days, intensity, and frequency [23,24]. However, extreme climate events can easily be triggered by abnormal climate backgrounds. It has been shown that abnormal weather conditions can lead to severe sandstorms in northern China [25]. During the winter of 2020–2021, a pronounced La Niña event occurred [26]. Against this background, severe dust weather occurred in northern China in mid-March 2021, with a duration of more than 4 days, an affected area of up to 3.8 million km^2, and the maximum accumulated dust concentration in the source area exceeding 18,000 $\mu g\ m^{-3}$. Visibility was less than 500 m in many areas, and Mongolia saw a large number of missing and injured people. Transportation and the socio-economic activities of several provinces in northern China were severely disrupted [27,28].

Extensive research has been conducted on the extreme dust event under investigation, focusing on its weather and climatic background as well as formation mechanisms [26,29]. However, limited literature exists regarding the transport characteristics of dust particles and their impact on PM_{10} and atmospheric visibility. Therefore, this study aims to address these gaps by examining the data and methods (Section 2), providing an overview of the weather conditions (Section 3), analyzing dust particle transport characteristics (Section 4), assessing the impact on air quality and visibility at multiple stations (Section 5), and presenting the discussion and conclusions.

2. Data and Methods

2.1. Data

This study utilizes the hourly fifth-generation European Center for Medium-Range Weather Forecasts (ERA5) reanalysis data [30] provided by ECMWF for weather background analysis (https://cds.climate.copernicus.eu/, access on 20 March 2023). The spatial resolution of wind, geopotential, and temperature at 200 hPa, 500 hPa, 700 hPa, and 850 hPa, as well as mean sea level pressure, is $0.25° \times 0.25°$ by latitude and longitude. The spatial resolution of 10 m-wind is $0.1° \times 0.1°$ by latitude and longitude. The study period covers from 12:00 on 14 March to 15:00 on 19 March 2021 (all times in Coordinated Universal Time, UTC).

When analyzing the dusting process, this study utilizes reanalysis data provided by CAMS (https://ads.atmosphere.copernicus.eu/, access on 20 March 2023), including parameters such as vertically integrated mass of dust aerosol (0.03–0.55 μm and 0.55–9 μm) and dust aerosol mixing ratio (0.03–0.55 μm and 0.55–9 μm). The spatial resolution is $0.75° \times 0.75°$ by latitude and longitude, and the temporal resolution is 3 h.

For analyzing the impact on air quality, this study utilizes hourly observations of PM_{10} and $PM_{2.5}$ concentrations obtained from the China National Environmental Monitoring Centre (http://www.cnemc.cn/, access on 20 March 2023), as well as maximum wind speed and minimum visibility data from the National Meteorological Information Center of the China Meteorological Administration (http://data.cma.cn/, access on 20 March 2023). Before analysis, the data undergoes rigorous quality control procedures, and a total of 245 monitoring stations with high-quality data are selected for subsequent statistical analysis.

2.2. Method of Determining the Location of Low-Pressure Center and Front

Cyclone center positioning using the Minimum Filtering Method. Within the dominant operational domain of the Mongolian cyclone (70–140° E, 45–60° N), a minimum filtering procedure is applied to the mean sea level pressure field. Subsequently, the position associated with the minimum pressure value is identified and designated as the center of the Mongolian cyclone. The application of smoothing techniques effectively eliminates minor noise, thus mitigating the risk of erroneous center detection and ensuring the accuracy of the results.

Frontal position determination using synoptic meteorological analysis. The frontal location is determined by analyzing the distribution of wind fields, temperature fields, pressure fields, and the arrangement of isobars and isotherms on surface weather maps. The presence of closely spaced isobars and isotherms near the frontal zone, along with isallotherm low and isallobaric high behind the cold front and isallotherm high and isallobaric low ahead of the warm front, are used as key criteria for identifying the position of the front.

2.3. Dust Duration and Classification, Air Quality Levels

Identification of the start and end times of the dust weather process. The criteria for determining the onset time of dust events, as specified by the Ministry of Ecology and Environment of the People's Republic of China (https://www.mee.gov.cn/, access on 20 March 2023), are as follows. The hourly PM_{10} concentration exceeds twice the average PM_{10} concentration of the previous 6 h and is greater than 150 μg m^{-3}, or the ratio of $PM_{2.5}$ to PM_{10} is less than or equal to 50% of the average ratio of the previous 6 h. The end time of a dust event is identified as the first instance when the PM_{10} concentration decreases to within a relative deviation of 10% from the average PM_{10} concentration of the 6 h preceding the occurrence of the dust event.

Identification of the level of dust weather. Referring to the national standard 'Classification of sand and dust weather' (GB/T 20480–2017) published by the China Meteorological Administration, visibility during sand and dust weather events is defined as ranging from 1 km to 10 km for blowing sand, less than 1 km for a sandstorm, and less than 500 m for a severe sandstorm.

Classification of Air Quality Index (AQI) Levels. The determination of AQI levels is based on the 'Technical Regulation on Ambient Air Quality Index (on trial)' (HJ 633–2012) published by the Ministry of Ecology and Environment of the People's Republic of China. The AQI corresponding to PM_{10} is calculated using the Individual Air Quality Index (IAQI) method. Based on the 24 h average PM_{10} mass concentration, pollution levels are categorized as Good (0–50 μg m^{-3}), Moderate (51–150 μg m^{-3}), Lower Pollution (151–250 μg m^{-3}), Medium Pollution (251–350 μg m^{-3}), Severe Pollution (351–420 μg m^{-3}), and Serious Pollution (>420 μg m^{-3}).

2.4. Study Area and Distribution of Observation Station

The study area encompasses the northern region of China (Figure 1), with the pink dots on the map indicating the locations of air quality monitoring stations. Two representative profiles (indicated by the solid yellow line) were selected to analyze the three-dimensional transport processes of dust based on the prevailing wind directions during dust weather events. To comprehensively assess the impact of this dust event on air quality in northern China, a number of representative sites (indicated by red pentagrams) from regions including northwest, northeast, and north China were chosen for analysis, including Ordos in Inner Mongolia, Tieling in Liaoning, Wuwei in Gansu, Tianjin, Anyang in Henan, Linyi in Shandong, Huainan in Anhui, and Xinyang in Henan. In the selection of representative sites, we try to make the distribution of sites in the study area broad and, combined with the main path of sand and dust transmission, more conducive to the study of the characteristics of dust transmission.

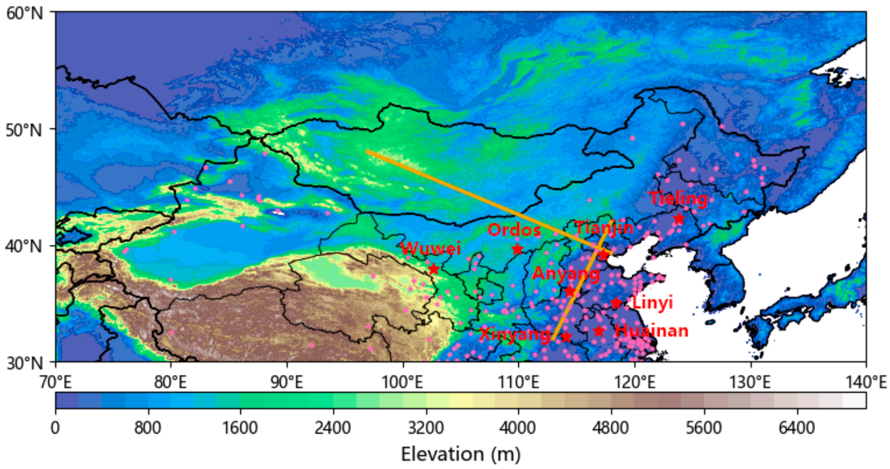

Figure 1. Study area and distribution of stations, including environmental monitoring stations (dots), representative urban stations (pentagrams), and representative profiles (solid yellow lines). The representative sites include Ordos in Inner Mongolia, Tieling in Liaoning, Wuwei in Gansu, Tianjin, Anyang in Henan, Linyi in Shandong, Huainan in Anhui, and Xinyang in Henan.

3. Weather Situation

Figure 2 presents the genesis and development process of the Mongolian cyclone. A thermal low-pressure system forms over the West Siberian Plain and rapidly propagates eastward to the border of Mongolia. Facilitated by the blocking of cold air and adiabatic warming from descending airflows, the Mongolian cyclone forms on the lee slopes of the Altai-Sayan mountain ranges. At 12:00 on the 14th, the cyclone enters the frontal stage, attains maturity, decelerates its movement, and reaches its maximum intensity after 12 h. Subsequently, the cyclone gradually weakens and eventually dissipates over the Sea of Japan. Next, the configuration of atmospheric circulation patterns at different levels, including 200 hPa, 500 hPa, 700 hPa, and sea level, will be examined to analyze their influence on sand initiation and dust transport.

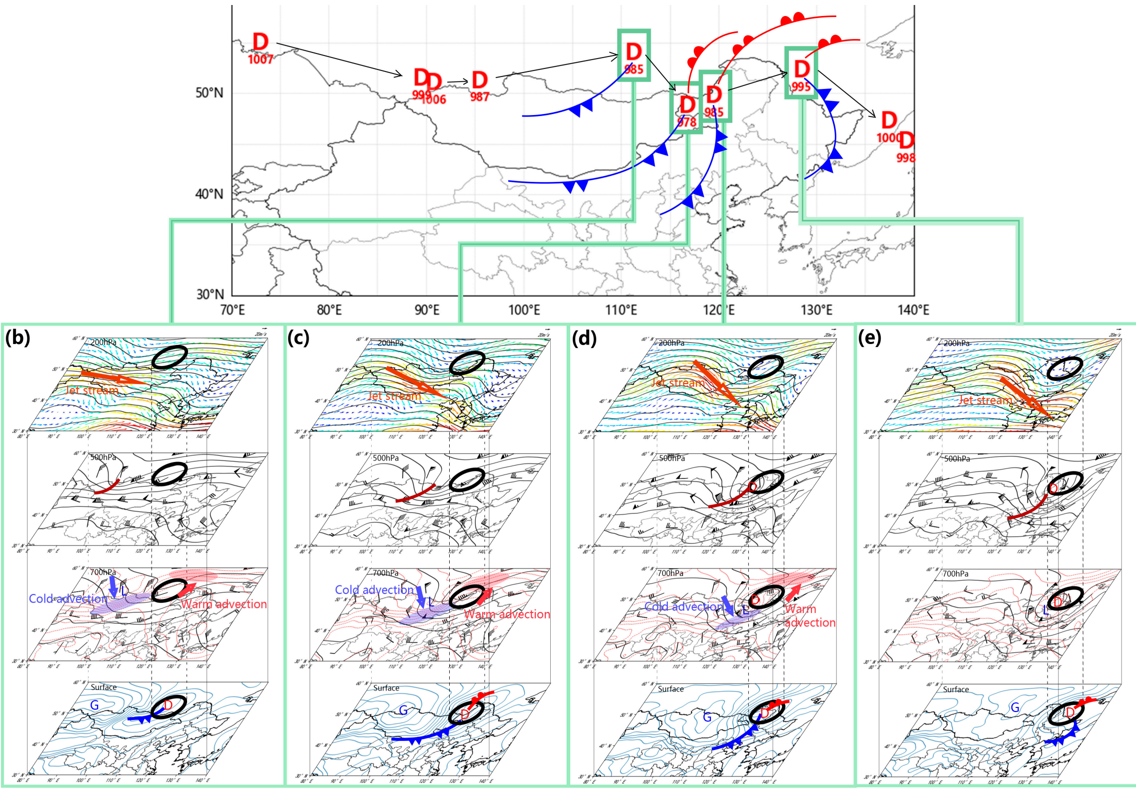

Figure 2. (**a**) Evolution of surface low pressure and front from 00:00 on 12 March to 12:00 on 16 March 2021, at 12 h intervals. High and low-level system configurations at (**b**) 00:00 on 14 March, (**c**) 12:00 on 14 March, (**d**) 00:00 on 15 March, and (**e**) 12:00 on 15 March 2021. The low-pressure center is represented by 'D', the high-pressure center by 'G', and the cold center by 'L'. The positions of surface cyclone centers are indicated by black circles. The figure shows the locations of cold and warm fronts, temperature advection, trough lines, and upper-level jet streams.

At the 500 hPa, a zonal circulation pattern characterized by 'two troughs and one ridge' is observed over the mid-high latitudes of the Eurasian continent. The temperature field exhibits a lag behind the geopotential field, facilitating the eastward development of the system due to pronounced horizontal pressure gradients. The upper-level trough intensifies and forms a closed circulation center on the lee side of the Mongolian Mountains, giving rise to the formation of a cold vortex with reduced translational speed. The most significant development occurs to the east of Lake Baikal (Figure 2c). Concurrently, a strong jet stream exceeding 50 m s^{-1} is present at 200 hPa over Mongolia to central Inner Mongolia (Figure 2b). On the left side of the jet exit region, a strong upper-level divergence field exists, providing favorable conditions for convergent upward motion. These dynamic conditions play a crucial role in the cyclone's development and facilitate the upward transport of sand particles.

At 700 hPa, cold air accumulates on the windward slope due to the diminishment caused by the Altai-Sayan mountains (Figure 2b). A frontal zone with densely distributed isotherms is observed near 50° N, and strong cold advection drives the southeastward movement of the cold front. Meanwhile, a warm tongue extends from the Tarim Basin towards the northeast, intersecting with the southward intrusion of cold advection from Siberia over Mongolia (Figure 2c), leading to the formation of a warm front and a frontal cyclone. The surface weather map reveals a Siberian high-pressure system with a strength exceeding 1035 hPa located behind the low-pressure center of the Mongolian cyclone. This generates a strong pressure gradient zone in the central part of Mongolia, resulting in a significant enhancement of near-surface wind speed. The intensified winds provide favorable dynamic conditions for the near-surface sand lifting processes.

Overall, the strong upper-level divergence on the left side of the jet exit region at 200 hPa, along with the strong positive vorticity advection ahead of the upper-level trough at 500 hPa, as well as the convergence of cold and warm advection at 700 hPa and near the surface, constitute a highly favorable configuration of the atmospheric circulation at different levels. These factors collectively promote the rapid development of the Mongolian cyclone. Furthermore, the evolution of the frontal cyclone system provides favorable dynamic conditions for the sand and dust process, including the significant surface winds promoting sand uplift, the convergence-induced upward motion facilitating the upward transport of sand and dust, and the strong winds at higher altitudes enabling long-distance transport of sand and dust.

4. Transport Characteristics of Dust

More frequent and intense vertical motion can lift dust particles into the upper level, prolonging their residence time in the atmosphere [31]. In this study, the vertically integrated mass of dust aerosol in the ranges of 0.03–0.55 μm and 0.55–9 μm, combined with wind fields greater than 4 m s^{-1}, is used to show the transport characteristics of pollutants during dust weather events on a two-dimensional plane.

Guided by the northwestern airflow in the rear of the Mongolian cyclone, the dust entered Inner Mongolia through the China–Mongolia border, resulting in a banded distribution of high dust concentrations in Inner Mongolia and the Northeast China Plain (Figure 3a,b). The southern edge of the dust zone was hindered by mountain ranges and difficult to diffuse. Convective motion in the vertical direction, along with strong winds associated with weather systems, facilitated the lifting of dust into the air, increasing the dust concentration in the atmospheric column. Gusts of more than 12 m s^{-1} were observed in multiple locations, causing dust to be transported downstream and deposited, resulting in dust weather events in China's northeast, northwest, and northern area. As the Mongolian cyclone weakened and moved eastward, the strong winds at the surface weakened. Affected by the return flow of the front of the Siberian cold high pressure, dust spread southward and eastward to the southern part of the North China Plain, including the Jiangsu and Anhui provinces (Figure 3e,f).

Meanwhile, under the influence of the northeast airflow in front of the Siberian cold high pressure, Xinjiang province also shows a relatively high concentration of dust. Surrounded by high mountains with an average elevation of over 5 km, the Tarim Basin is dominated by easterly and northeasterly winds throughout the year [32]. Therefore, the dust in this place is difficult to dissipate below an altitude of 5 km, and a relatively stable dust-closed circulation is formed in this place. In addition, the local supply of sand sources, such as the Taklamakan Desert, led to a sustained high concentration of dust.

Due to the rapid movement of the Mongolia cyclone and the front (Figure 2), the upward motion ahead of the cold front is conducive to the suspension of dust aerosols in the boundary layer, while the strong sinking motion behind the cold front leads to the accumulation of cold air, causing the dust to settle in downstream areas [14]. This results in surface-divergent winds, highlighting the importance of vertical motion in the analysis of dust weather. The dust aerosol mixing ratio represents the proportion of dust aerosol mass in unit dry air mass and can further demonstrate the stratification effect of the vertically integrated mass of dust aerosols (Figure 3). Therefore, this paper selects the mixing ratio from the ground to 400 hPa and chooses two profiles in the northwest–southeast (Figure 4a–f) and northeast–southwest (Figure 4g–l) directions, respectively, based on the dust transmission path. We analyzed the intensity and path of this sandstorm's overseas transport by its vertical motion characteristics. By combining the near-surface air pollution situation, we analyze the impact of sandstorms on air quality after entering China.

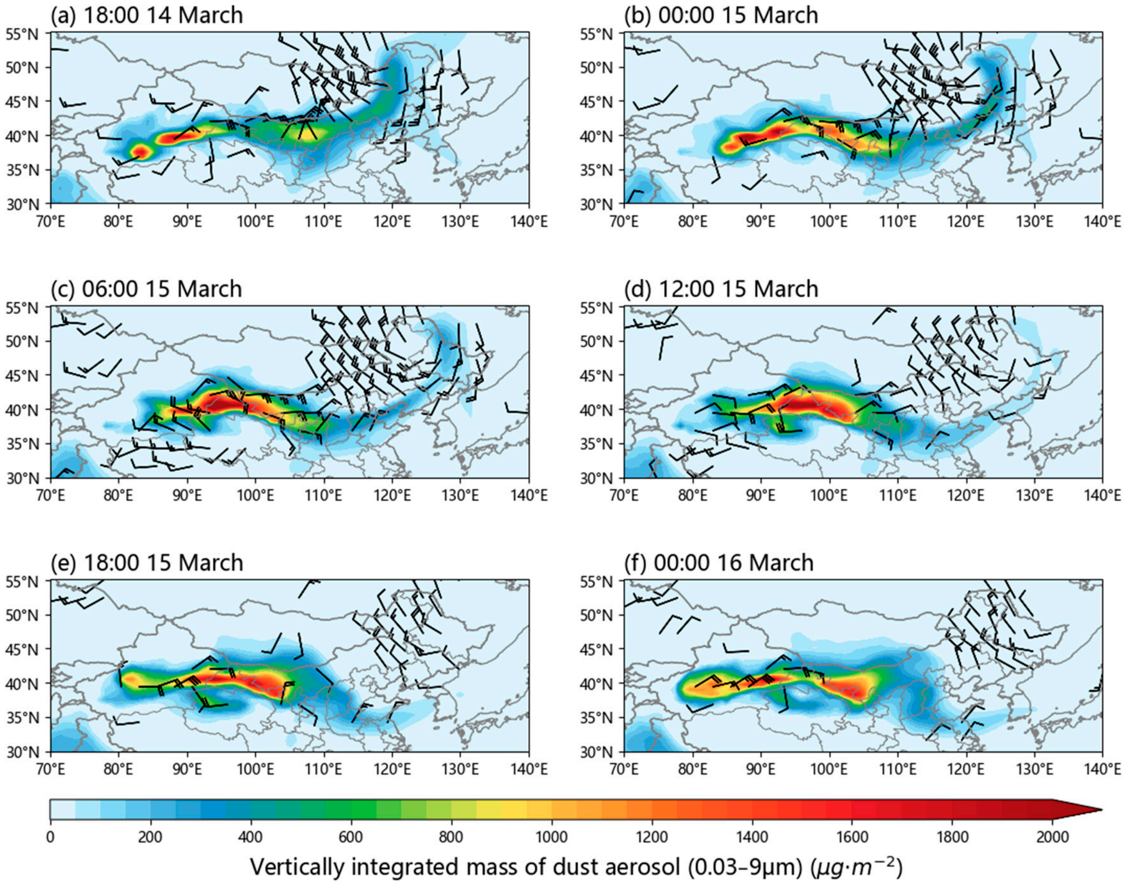

Figure 3. Vertically integrated mass of dust aerosols (unit: μg m^{-2}, shading) and wind vectors (unit: m s^{-1}, barb) over northern China. ((**a**) 18:00 on 14 March, (**b**) 00:00 on 15 March, (**c**) 06:00 on 15 March, (**d**) 12:00 on 15 March, (**e**) 18:00 on March 15, (**f**) 00:00 on 16 March).

At 18:00 on the 14th (Figure 4a), the sandstorm covered the air over central and western Mongolia and central Inner Mongolia, accompanied by a sinking motion zone with wind speeds exceeding 0.5 Pa s^{-1}. This resulted in dust settling and PM_{10} concentrations exceeding the upper observation threshold in many areas of Inner Mongolia. Twelve hours later, the sandstorm near the Altai Mountains was separated from the surface by updrafts and carried away, rapidly increasing again (Figure 4c). It was then transported over long distances into China by the northwestern flow provided by the cyclone's rear.

Affected by the northeast airflow ahead of the Siberian cold high, the sandstorm was transported southward after entering China. Under the influence of downdrafts and the gravitational settling of dust particles, the ground-level PM_{10} concentration increased sharply. Comparing the time of the increase in the vertical total dust amount with that of the increase in the ground-level PM_{10} concentration, we found that the ground air pollution lagged by about 12 h. Moreover, due to the dust from Mongolia being lifted again to supplement the dust from the upper levels to the North China Plain (Figure 4l), China continues to be affected by the dust.

In summary, the center of maximum intensity of this sandstorm was more than 2500 m away from the underlying surface, and the vertical influence range exceeded 4200 m. Sandstorms in North China and Northeast China were mainly caused by northwest winds passing through behind the cold front, while sandstorms in the southern part of the North China Plain were mainly caused by the southward diffusion of high-level sandstorms that had not dissipated and the sandstorm return caused by the eastward airflow.

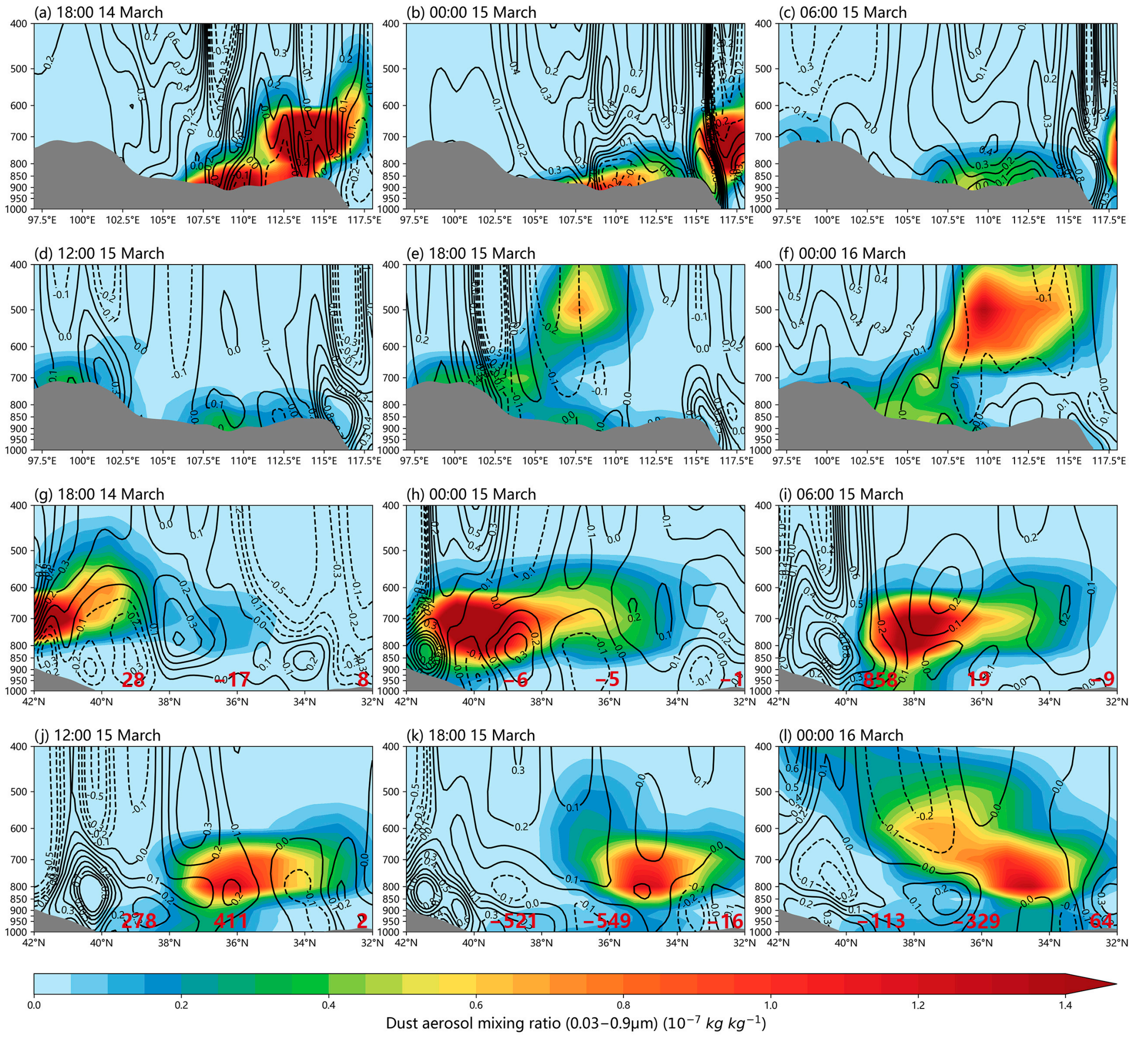

Figure 4. The profile along the dust path (yellow line in Figure 1) shows the vertical velocity (unit: Pa s^{-1}, contours) and the dust aerosol mixing ratio (0.03–0.9 μm) (unit: 10^{-7} kg kg^{-1}, shading). Figures (**a**–**f**) depict the dust path from (48° N, 97° E) to (39.3° N, 118.0° E). Figures (**g**–**l**) draw the dust path from (42.0° N, 118.0° E) to (32.0° N, 113.0° E). The red numbers at the bottom represent the change in PM_{10} concentration (unit: μg m^{-3}) over a 3 h period at three stations, respectively: Tianjin, Anyang, and Xinyang arranged from north to south.

5. Effects on Air Quality

5.1. Spatial Distribution of Particulate Matter (PM)

Figure 5 depicts the spatial distribution of PM_{10} concentrations at air quality monitoring stations at 6 h intervals. Starting from 15 March, regions with high PM_{10} concentrations were concentrated in the eastern part of Xinjiang, central-western Inner Mongolia, and the Hexi Corridor (Figure 5a,b). Subsequently, the affected area rapidly expanded, extending towards the Hetao region, the middle and lower reaches of the Yellow River, and dispersing towards the Huang-Huai region, reaching as far south as the northern parts of Jiangsu and Anhui provinces (Figure 5c–f). Due to the obstruction caused by the Tibet Plateau, particulate matter accumulated on the eastern side of the plateau, resulting in sustained high concentrations.

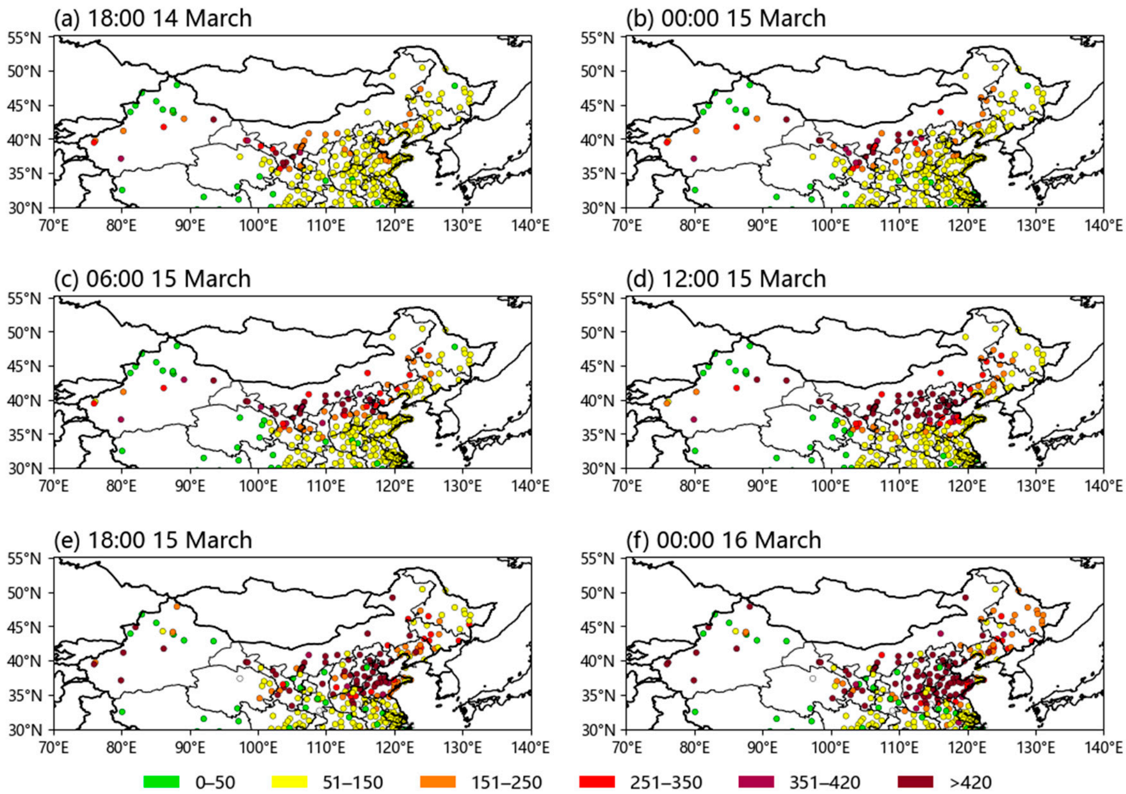

Figure 5. Spatial distribution of 24 h average PM_{10} mass concentrations (unit: μg m^{-3}, scatter) at air quality monitoring stations in northern China. ((**a**) 18:00 on 14 March 2021, (**b**) 00:00 on 15 March, (**c**) 06:00 on 15 March, (**d**) 12:00 on 15 March, (**e**) 18:00 on 15 March, (**f**) 00:00 on 16 March).

Table 1 provides statistical results for the pollution event. The 'Num' column and 'Num_12h' column represent the number of monitoring stations corresponding to each pollution level and the number of stations with pollution duration exceeding 12 h, respectively. 'Proportion' and 'Proportion_12h' indicate the proportion of the aforementioned station categories to the total number of stations. As of 00:00 on the 16th, 4.9% of the monitoring stations in northern China exhibited severe pollution, while 31.4% of the stations were significantly affected, reaching the level of serious pollution. Stations experiencing medium and lower pollution accounted for 8.2% and 14.3% of the total, respectively. The statistical analysis reveals that this intense sand and dust event affected 58.8% of the stations in northern China, with 36.3% of the stations experiencing severe pollution or higher. In terms of duration, a substantial proportion of the stations, 35.9%, experienced pollution for more than 12 h. Among them, the highest proportion was observed in stations affected by severe pollution, accounting for 16.3%. The next highest proportion was in stations affected by lower pollution, accounting for 10.6%. Stations affected by medium and severe pollution accounted for 5.3% and 3.7%, respectively. These results highlight the severe air pollution caused by this event in northern China, with extreme intensity, extensive coverage, and a prolonged duration compared to previous historical cases.

The temporal evolution of surface PM_{10} concentrations, as depicted in Figure 5, exhibits a pattern similar to the evolution of total atmospheric column dust mass shown in Figure 3, albeit with a certain time lag. Analysis indicates that dust particles are initially transported to higher altitudes, resulting in an increase in the overall dust mass within the atmospheric column (Figure 3a), while surface contamination remains relatively low. As demonstrated in Figure 4c,i, the dust particles subsequently propagate downstream and deposit, leading to a significant increase in pollutant concentrations at ground-level monitoring stations, ultimately causing pollution events in Northwestern China, North China, and Northeast China (Figure 5c–f). Therefore, it can be concluded that the increase in pollutant concentrations near the surface lags behind the increase in total dust mass within the atmospheric column, as the dispersion and settling processes of pollutants require a certain amount of time. Similarly, the dissipation of pollution lags behind the cessation of the dusting process.

Table 1. Statistical table of the pollution situation in northern China stations from 18:00 on March 14 to 00:00 on March 16, 2021.

PM_{10}_24 h ($\mu g\ m^{-3}$)	Pollution Level	Num	Proportion	Num_12 h	Proportion_12 h
0–150	No pollution	101	41.2%	0	0
151–250	Lower	35	14.3%	26	10.6%
251–350	Medium	20	8.2%	13	5.3%
351–420	Severe	12	4.9%	9	3.7%
>420	Serious	77	31.4%	40	16.3%
Total		245	100%	88	35.9%

5.2. Temporal Variation of PM and Meteorological Elements at Typical Stations

To provide a more comprehensive assessment of the influence of this dust event on air quality and visibility, a detailed analysis will be conducted at eight selected urban stations. These stations encompass a range of parameters, including PM_{10}, $PM_{2.5}$, wind speed, relative humidity, and visibility, which will be examined in depth.

Under the influence of northwest airflow in the rear of the cyclone, the sandstorm entered China across the border with Inner Mongolia. Ordos was the first to be affected by the pollution at 19:00 on the 14th (Figure 6a), with its PM_{10} concentration rising to the upper observation threshold (9985 $\mu g\ m^{-3}$) within one hour. The minimum visibility was 183 m, and the strong sandstorm persisted for 9 consecutive hours. Meanwhile, the northeast airflow in front of the Siberian high pressure affected the Hexi Corridor, which is adjacent to the Tengger Desert, an abundant source of sand. Due to the obstruction of the mountains, the sand in Wuwei was not easily dispersed (Figure 6b), and the severe sandstorm weather lasted for more than 13 h, with the sandstorm weather ending on the 19th.

Tianjin and Tieling are located in plains, and strong winds favor the horizontal dispersion of pollutants. The sandstorm event in these two areas lasted for approximately 24 h (Figure 6c,d). Before the front passes, liquid PM significantly affects visibility. This, combined with the dust, caused low visibility in Tianjin. However, precipitation has a scavenging activity on pollutants in the air, so after experiencing a brief period of blowing sand, Tieling's visibility improved continuously.

After long-distance transport, the intensity of the dust weakened, and the dust intensity in the southern part of the North China Plain was categorized as 'floating dust'. Anyang and Linyi, which are located at similar latitudes, experienced dust events with little time difference (Figure 6e,f). However, the PM_{10} concentration curve in Linyi showed a bimodal feature, which may be due to the obstruction of the Shandong Hills upstream, resulting in a brief decline in the local particle concentration during the dust event. Xinyang and Huainan are located near the Middle and Lower Yangtze River Plain, and both were affected by dust on the 16th (Figure 6g,h). There is a significant inverse correlation between the relative humidity and visibility curve before the front passes, and liquid PM significantly affects atmospheric visibility at this stage. As the front passes through, although the concentration of PM_{10} increases, visibility slowly increases, which is related to the wet deposition caused by precipitation processes. Therefore, the impact of liquid PM on visibility at southern stations is greater. The dust impact periods of Tianjin, Anyang, and Xinyang stations correspond well with the dust transport processes in the vertical profile (Figure 4). The starting times at adjacent sites differ by about 12 h, which can provide a reference for downstream areas when forecasting dust weather.

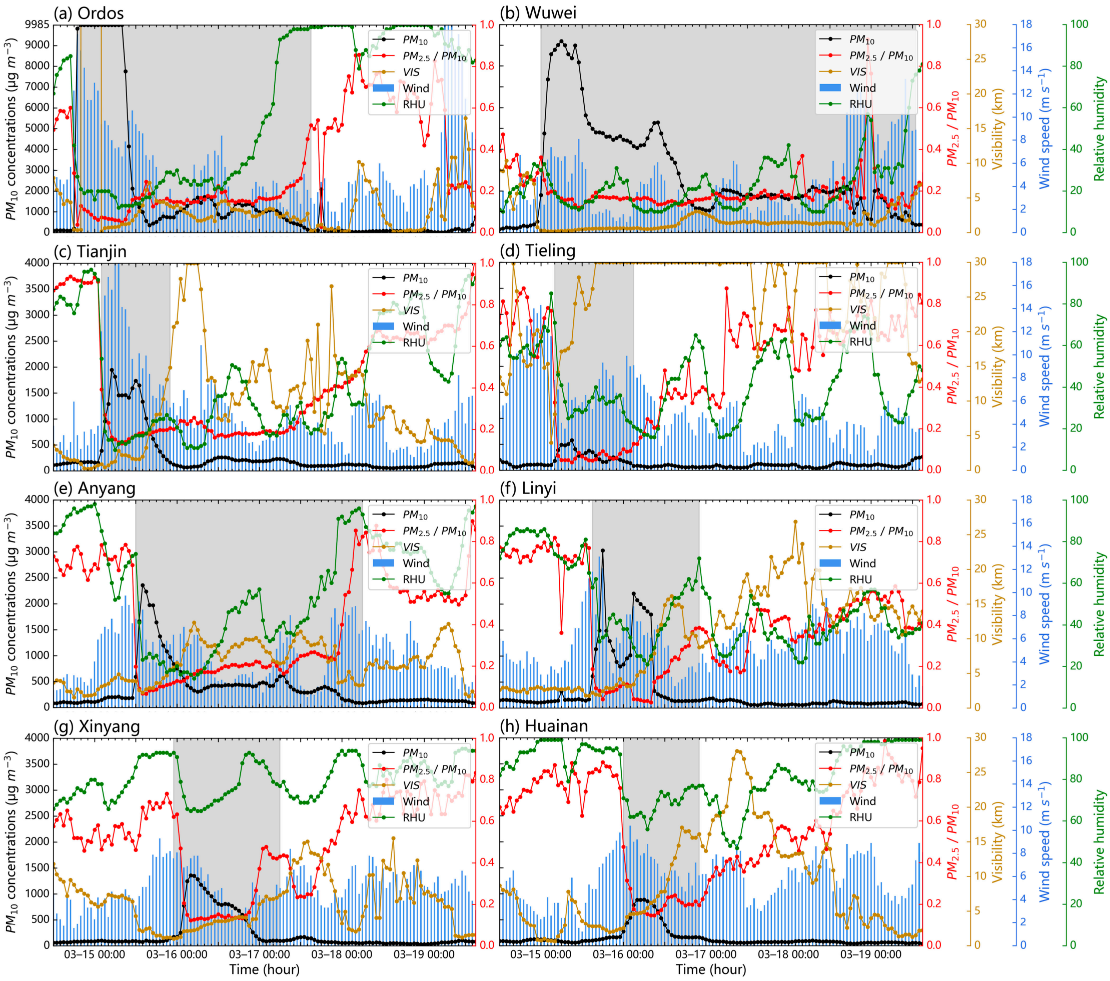

Figure 6. From 12:00 on 14 March to 15:00 on 19 March, the hourly variations of PM_{10} mass concentration (unit: μg m^{-3}, black line), the ratio of $PM_{2.5}$ to PM_{10} (red line), visibility (unit: m, yellow line), relative humidity (green line), and wind speed (unit: m s^{-1}, blue bar) were recorded at monitoring sites in (**a**) Ordos, (**b**) Wuwei, (**c**) Tianjin, (**d**) Tieling, (**e**) Anyang, (**f**) Linyi, (**g**) Xinyang, and (**h**) Huainan. The shaded areas represent the occurrence of dust events.

In summarizing the analysis results for the eight representative stations in conjunction with the frontal passage process, several significant observations can be made. During the frontal passage, strong winds exceeding 10 m s^{-1}, with a maximum reaching 18 m s^{-1}, are commonly observed near the surface. Subsequently, the occurrence of dust weather leads to a rapid increase in PM_{10} hourly concentration, accompanied by a pronounced decrease in the proportion of $PM_{2.5}$ within PM_{10}. This indicates that the transported dust primarily consists of particles with aerodynamic diameters of 2.5–10 μm. The impact on visibility is found to be multifaceted. Stations in close proximity to the dust source experience a swift reduction in visibility upon the arrival of dust, highlighting the significant influence of solid dust particles through 'fast processes'. In contrast, stations located further south with relatively moist and favorable precipitation conditions exhibit a clear inverse correlation between relative humidity and visibility before the frontal passage. Liquid particles play a noteworthy role in affecting atmospheric visibility during this stage. Despite an increase in PM_{10} concentration, visibility shows a gradual improvement as the frontal passage progresses, which can be attributed to the wet deposition induced by precipitation. Therefore, in southern stations, the impact of liquid particles on visibility is more pronounced.

6. Conclusions

This study presents an analysis of a severe dust event that occurred in March 2021. The analysis is based on meteorological parameters derived from the ERA5 reanalysis dataset, atmospheric composition data from the CAMS reanalysis dataset, as well as meteorological elements and air quality monitoring data from surface stations in China. The study examines the impact of this dust event on air quality and atmospheric visibility. The main findings of this research are as follows.

1. The present dust event belongs to the typical Mongolian cyclone-induced type. The strong divergence on the left side of the jet stream exit, the positive vorticity advection ahead of the trough at high levels, and the strong temperature gradient at low levels all contribute to the initiation and development of the frontal cyclone system. The intense Mongolian cyclone facilitates near-surface dust uplift and promotes both vertical and long-distance horizontal transport of dust, thereby providing advantageous dynamic conditions for this dust event.
2. The Gobi Desert in Mongolia is the primary source, with dust particles transported from Mongolia to northern China via the northwesterly flow behind the Mongolian cyclone. The dust event lags behind the evolution of weather systems. The Mongolian cyclone induces vertical motion in the lower atmosphere, uplifting and transporting near-surface dust particles. The dust transport displays a complex three-dimensional structure; the maximum dust intensity occurs at around 2500 m, characterized by a wide and elevated region of high values extending vertically, with some areas reaching over 4200 m.
3. This dust event has a significant impact on air quality in northern China, characterized by its extensive spatial coverage, high intensity, and prolonged duration. A total of 58.8% of the monitoring sites in northern China were affected by the pollution, with 36.3% of the sites reaching severe pollution levels or higher. Furthermore, 35.9% of the sites experienced more than 12 h of pollution. With the arrival of a sandstorm, the concentration of PM_{10} rapidly increases; this indicates that the contribution of external dust sources to PM_{10} particles is dominant.
4. The visibility is primarily affected by solid dust particles, especially at the northern stations, which are closer to the dust source. The increase in the PM_{10} concentration leads to a rapid reduction in visibility. However, the southern stations, characterized by higher moisture content, exhibit a clear inverse correlation between relative humidity and visibility, indicating a significant influence of liquid particles on visibility before the frontal passage. Subsequently, the visibility gradually improves due to the wet deposition resulting from the precipitation process.

This study has analyzed a single extreme case, which limits the generalizability of the results. Further analysis of multiple extreme events is needed for broader conclusions. Additionally, regarding air quality, this study has only focused on inhalable PM, while changes in atmospheric components such as ozone, nitrogen oxides, and sulfur compounds can also contribute to air quality degradation and pose health risks. Subsequent research will incorporate analysis of these variables to obtain a more comprehensive understanding of the subject matter.

Author Contributions: X.L.: Conceptualization, data curation, software, visualization, writing—original draft, writing—review and editing. Y.Z.: Conceptualization, supervision, writing—review and editing. H.Y.: Software and visualization. Q.L.: Writing—review and editing. J.X.: Conceptualization and supervision. All authors have read and agreed to the published version of the manuscript.

Funding: This research was funded by the Major Research Plan of the National Natural Science Foundation of China (grant number 72293604), the Program for Scientific Research Start-Up Funds of Guangdong Ocean University (101302/R17061), the Guangdong Provincial College Innovation Team Project (2019KCXTF021) and the First-Class Discipline Plan of Guangdong Province (080503032101 and 231420003).

Data Availability Statement: All data for this study are available from the corresponding author on request.

Acknowledgments: We thank the European Centre, the Copernicus Centre, the China National Environmental Monitoring Centre, and the China Meteorological Administration for their valuable data support, which greatly contributed to this research.

Conflicts of Interest: The authors declare no conflict of interest.

References

1. Han, H.; Guo, L.; Zhang, J.Q.; Zhang, K.Z.; Cui, N.B. Spatiotemporal analysis of the coordination of economic development, resource utilization, and environmental quality in the Beijing-Tianjin-Hebei urban agglomeration. *Ecol. Indic.* **2021**, *127*, 107724. [CrossRef]
2. Zhao, L.; Liu, C.; Liu, X.; Liu, K.; Shi, Y. Urban spatial structural options for air pollution control in China: Evidence from provincial and municipal levels. *Energy Rep.* **2021**, *7*, 93–105. [CrossRef]
3. Zhang, Q.; Meng, X.; Shi, S.; Kan, L.; Chen, R.; Kan, H. Overview of particulate air pollution and human health in China: Evidence, challenges, and opportunities. *Innovation* **2022**, *3*, 100312. [CrossRef] [PubMed]
4. Wang, Z.; Hu, B.; Zhang, C.; Atkinson, P.M.; Wang, Z.; Xu, K.; Chang, J.; Fang, X.; Jiang, Y.; Shi, Z. How the Air Clean Plan and carbon mitigation measures co-benefited China in PM2.5 reduction and health from 2014 to 2020. *Environ. Int.* **2022**, *169*, 107510. [CrossRef] [PubMed]
5. Zheng, Y.; Xue, T.; Zhao, H.; Lei, Y. Increasing life expectancy in China by achieving its 2025 air quality target. *Environ. Sci. Ecotechnol.* **2022**, *12*, 100203. [CrossRef] [PubMed]
6. Querol, X.; Tobias, A.; Perez, N.; Karanasiou, A.; Amato, F.; Stafoggia, M.; Perez Garcia-Pando, C.; Ginoux, P.; Forastiere, F.; Gumy, S.; et al. Monitoring the impact of desert dust outbreaks for air quality for health studies. *Environ. Int.* **2019**, *130*, 104867. [CrossRef]
7. Chen, S.; Huang, J.; Kang, L.; Wang, H.; Ma, X.; He, Y.; Yuan, T.; Yang, B.; Huang, Z.; Zhang, G. Emission, transport, and radiative effects of mineral dust from the Taklimakan and Gobi deserts: Comparison of measurements and model results. *Atmos. Chem. Phys.* **2017**, *17*, 2401–2421. [CrossRef]
8. Chen, S.; Huang, J.; Li, J.; Jia, R.; Jiang, N.; Kang, L.; Ma, X.; Xie, T. Comparison of dust emissions, transport, and deposition between the Taklimakan Desert and Gobi Desert from 2007 to 2011. *Sci. China Earth Sci.* **2017**, *60*, 1338–1355. [CrossRef]
9. Li, J.; Hao, X.; Liao, H.; Yue, X.; Li, H.; Long, X.; Li, N. Predominant Type of Dust Storms That Influences Air Quality Over Northern China and Future Projections. *Earths Future* **2022**, *10*, e2022EF002649. [CrossRef]
10. Xu, C.; Guan, Q.; Lin, J.; Luo, H.; Yang, L.; Tan, Z.; Wang, Q.; Wang, N.; Tian, J. Spatiotemporal variations and driving factors of dust storm events in northern China based on high-temporal-resolution analysis of meteorological data (1960–2007). *Environ. Pollut.* **2020**, *260*, 114084. [CrossRef]
11. Zhang, T.; Zheng, M.; Sun, X.; Chen, H.; Wang, Y.; Fan, X.; Pan, Y.; Quan, J.; Liu, J.; Wang, Y.; et al. Environmental impacts of three Asian dust events in the northern China and the northwestern Pacific in spring 2021. *Sci. Total Environ.* **2023**, *859*, 160230. [CrossRef] [PubMed]
12. Zhang, W.; Zhuang, G.; Huang, K.; Li, J.; Zhang, R.; Wang, Q.; Sun, Y.; Fu, J.S.; Chen, Y.; Xu, D.; et al. Mixing and transformation of Asian dust with pollution in the two dust storms over the northern China in 2006. *Atmos. Environ.* **2010**, *44*, 3394–3403. [CrossRef]
13. Tan, S.; Chen, B.; Wang, H.; Che, H.; Yu, H.; Shi, G. Variations in Aerosol Optical Properties over East Asian Dust Storm Source Regions and Their Climatic Factors during 2000–2021. *Atmosphere* **2022**, *13*, 992. [CrossRef]
14. Ridley, D.A.; Heald, C.L.; Kok, J.F.; Zhao, C. An observationally constrained estimate of global dust aerosol optical depth. *Atmos. Chem. Phys.* **2016**, *16*, 15097–15117. [CrossRef]
15. Singh, C.; Singh, S.K.; Chauhan, P.; Budakoti, S. Simulation of an extreme dust episode using WRF-CHEM based on optimal ensemble approach. *Atmos. Res.* **2021**, *249*, 105296. [CrossRef]
16. Kim, K.-M.; Kim, S.-W.; Choi, M.; Kim, M.; Kim, J.; Shin, I.; Kim, J.; Chung, C.-Y.; Yeo, H.; Kim, S.-W.; et al. Modeling Asian Dust Storms Using WRF-Chem During the DRAGON-Asia Field Campaign in April 2012. *J. Geophys. Res. Atmos.* **2021**, *126*, e2021JD034793. [CrossRef]
17. Akritidis, D.; Pozzer, A.; Flemming, J.; Inness, A.; Zanis, P. A Global Climatology of Tropopause Folds in CAMS and MERRA-2 Reanalyses. *J. Geophys. Res. Atmos.* **2021**, *126*, e2020JD034115. [CrossRef]
18. Inness, A.; Ades, M.; Agusti-Panareda, A.; Barre, J.; Benedictow, A.; Blechschmidt, A.-M.; Dominguez, J.J.; Engelen, R.; Eskes, H.; Flemming, J.; et al. The CAMS reanalysis of atmospheric composition. *Atmos. Chem. Phys.* **2019**, *19*, 3515–3556. [CrossRef]
19. Xie, Z.; Cheng, Z.; Bueh, C.; Yong, M.; Wu, C.; Gomboluudev, P. Pattern Transition of Dust Events over Northern China and Mongolia and Its Modulating Circulation in Spring. *Sola* **2022**, *18*, 159–166. [CrossRef]
20. Chen, L.; Li, D.; Pryor, S.C. Wind speed trends over China: Quantifying the magnitude and assessing causality. *Int. J. Climatol.* **2013**, *33*, 2579–2590. [CrossRef]
21. Tai, A.P.K.; Ma, P.H.L.; Chan, Y.-C.; Chow, M.-K.; Ridley, D.A.; Kok, J.F. Impacts of climate and land cover variability and trends on springtime East Asian dust emission over 1982–2010: A modeling study. *Atmos. Environ.* **2021**, *254*, 118348. [CrossRef]

22. Guan, Q.; Yang, J.; Zhao, S.; Pan, B.; Liu, C.; Zhang, D.; Wu, T. Climatological analysis of dust storms in the area surrounding the Tengger Desert during 1960–2007. *Clim. Dyn.* **2015**, *45*, 903–913. [CrossRef]
23. An, L.; Che, H.; Xue, M.; Zhang, T.; Wang, H.; Wang, Y.; Zhou, C.; Zhao, H.; Gui, K.; Zheng, Y.; et al. Temporal and spatial variations in sand and dust storm events in East Asia from 2007 to 2016: Relationships with surface conditions and climate change. *Sci. Total Environ.* **2018**, *633*, 452–462. [CrossRef] [PubMed]
24. Wu, C.; Lin, Z.; Shao, Y.; Liu, X.; Li, Y. Drivers of recent decline in dust activity over East Asia. *Nat. Commun.* **2022**, *13*, 7105. [CrossRef] [PubMed]
25. Xu, X.; Zhao, T.; Liu, F.; Gong, S.L.; Kristovich, D.; Lu, C.; Guo, Y.; Cheng, X.; Wang, Y.; Ding, G. Climate modulation of the Tibetan Plateau on haze in China. *Atmos. Chem. Phys.* **2016**, *16*, 1365–1375. [CrossRef]
26. Yin, Z.; Wan, Y.; Zhang, Y.; Wang, H. Why super sandstorm 2021 in North China? *Natl. Sci. Rev.* **2022**, *9*, nwab165. [CrossRef]
27. Severe Sand and Dust Storm Hits Asia. Available online: https://public.wmo.int/en/media/news/severe-sand-and-dust-storm-hits-asia (accessed on 16 March 2021).
28. Liang, L.; Han, Z.; Li, J.; Xia, X.; Sun, Y.; Liao, H.; Liu, R.; Liang, M.; Gao, Y.; Zhang, R. Emission, transport, deposition, chemical and radiative impacts of mineral dust during severe dust storm periods in March 2021 over East Asia. *Sci. Total Environ.* **2022**, *852*, 158459. [CrossRef]
29. Jin, J.; Pang, M.; Segers, A.; Han, W.; Fang, L.; Li, B.; Feng, H.; Lin, H.X.; Liao, H. Inverse modeling of the 2021 spring super dust storms in East Asia. *Atmos. Chem. Phys.* **2022**, *22*, 6393–6410. [CrossRef]
30. Hersbach, H.; Bell, B.; Berrisford, P.; Hirahara, S.; Horanyi, A.; Munoz-Sabater, J.; Nicolas, J.; Peubey, C.; Radu, R.; Schepers, D.; et al. The ERA5 global reanalysis. *Q. J. R. Meteorol. Soc.* **2020**, *146*, 1999–2049. [CrossRef]
31. Zhang, Z.; Zhang, X.; Gong, D.; Kim, S.J.; Mao, R.; Zhao, X. Possible influence of atmospheric circulations on winter haze pollution in the Beijing-Tianjin-Hebei region, northern China. *Atmos. Chem. Phys.* **2016**, *16*, 561–571. [CrossRef]
32. Huang, J.; Wang, T.; Wang, W.; Li, Z.; Yan, H. Climate effects of dust aerosols over East Asian arid and semiarid regions. *J. Geophys. Res. Atmos.* **2014**, *119*, 11398–11416. [CrossRef]